Comprehensive measurement of *pp*-chain solar neutrinos

The Borexino Collaboration*

About 99 per cent of solar energy is produced through sequences of nuclear reactions that convert hydrogen into helium, starting from the fusion of two protons (the *pp* chain). The neutrinos emitted by five of these reactions represent a unique probe of the Sun's internal working and, at the same time, offer an intense natural neutrino beam for fundamental physics. Here we report a complete study of the *pp* chain. We measure the neutrino–electron elastic-scattering rates for neutrinos produced by four reactions of the chain: the initial proton–proton fusion, the electron-capture decay of beryllium-7, the three-body proton–electron–proton (*pep*) fusion, here measured with the highest precision so far achieved, and the boron-8 beta decay, measured with the lowest energy threshold. We also set a limit on the neutrino flux produced by the ^{3}He–proton fusion (hep). These measurements provide a direct determination of the relative intensity of the two primary terminations of the *pp* chain (*pp*-I and *pp*-II) and an indication that the temperature profile in the Sun is more compatible with solar models that assume high surface metallicity. We also determine the survival probability of solar electron neutrinos at different energies, thus probing simultaneously and with high precision the neutrino flavour-conversion paradigm, both in vacuum and in matter-dominated regimes.

In 1937, Gamov and von Weizsäcker[1,2] suggested that the Sun is powered by a chain of nuclear reactions initiated by proton–proton fusion and leading to the production of ^{4}He. This idea was further developed by Bethe and Critchfield[3]. At about the same time von Weizsäcker and independently Bethe proposed an alternative mechanism, namely the carbon–nitrogen–oxygen cycle (CNO cycle)[4], a closed-loop chain of nuclear reactions catalysed by ^{12}C, ^{14}N and ^{16}O nuclei in which four protons are converted into ^{4}He. Although the CNO cycle was incorrectly considered to be the main source of energy in the Sun (mainly because of the overestimation of the Sun's central temperature available at that time), the debate on the role of the CNO cycle in the Sun is still relevant today. Indeed, a direct measure of its importance is missing, although theory predicts that it cannot contribute more than about 1% of the solar luminosity. Conversely, it is now understood to be the main source of energy in stars heavier than the Sun. More historical details can be found in ref. [5].

The Sun and lower-mass stars are predominantly powered by the *pp* chain (see Fig. 1), which has been thoroughly studied by Fowler and co-workers in the 1950s[6]. He and A. Cameron also pointed out that the detection of solar neutrinos could be a direct way of testing theoretical solar models. Their intuition was correct and neutrinos are now considered to be the sole direct probes of the Sun's core and of solar energy generation.

Neutrinos are copiously emitted in the primary *pp* fusion reaction of the chain and, to a minor extent, in the alternative three-body *pep* process and in the two secondary branches *pp*-II (^{7}Be neutrinos) and *pp*-III (^{8}B neutrinos). Experimentally, solar neutrinos have been studied since the late 1960s by radiochemical experiments (Homestake[7], SAGE[8] and GALLEX[9]) which, however, could only provide a measurement of their integrated flux on Earth above a threshold. Prior to the establishment of the Borexino project, only ^{8}B neutrinos (<0.01% of the total flux) have been measured individually by KamiokaNDE/SuperKamiokande[10] and the Sudbury Neutrino Observatory (SNO)[11]. Their measurements have definitively proved that neutrinos undergo leptonic flavour (that is, electronic, muonic or tauonic) conversion in the Sun's matter, enhanced through the MSW (Mikheyev–Smirnov–Wolfenstein) mechanism[12–14]. For an historical review of solar-neutrino astronomy and of its impact on solar and neutrino physics see, for example, refs [15–17].

The measurement of all neutrino components is the most direct way to test the standard solar model (SSM)[15] and to validate our theoretical understanding of the properties of the Sun's core. The first theoretical predictions of neutrino fluxes were made in the 1960s by J. Bahcall and his collaborators and have subsequently been refined by many theoretical groups[18]. Despite the results delivered by solar-neutrino experiments, important questions about the Sun remain unanswered. For example, the solar metallicity, that is, the abundance of elements heavier than He, is poorly understood, even though it is a fundamental parameter for the determination of the physical properties of the Sun. A precise measurement of the solar neutrino fluxes comprising the *pp* chain and the CNO cycle would directly settle the controversy between high-metallicity (HZ) and low-metallicity (LZ) SSMs[18] (see Methods). This study is a step in this direction.

Solar neutrinos are also powerful probes of neutrino properties. First, they allow the determination of oscillation parameters, especially the θ_{12} mixing angle and, to a lesser degree, the Δm^2_{12} mass splitting. Second, the measurement of the electron neutrino survival probability (P_{ee}) as a function of neutrino energy allows us to probe directly the MSW-LMA mechanism of neutrino oscillations[19] and to search for deviations that could indicate the presence of physics beyond the standard model.

Running continuously since 2007, the Borexino experiment has measured, one after another, ^{7}Be neutrinos[20–22], *pep* neutrinos[23], ^{8}B neutrinos[24] and *pp* neutrinos[25]. Here we report the simultaneous precision spectroscopic measurement of the complete *pp* chain and its implications for both solar and neutrino physics.

Borexino and the solar-neutrino analysis

Borexino is a liquid-scintillator experiment at the Laboratori Nazionali del Gran Sasso in Italy[26]. Given the tiny cross-section of neutrino interactions with electrons ($\sigma \approx 10^{-44}$ cm^2 to 10^{-45} cm^2 for the solar-neutrino energy range), the rates expected in Borexino are small,

*A list of participants and their affiliations appears at the end of the paper.

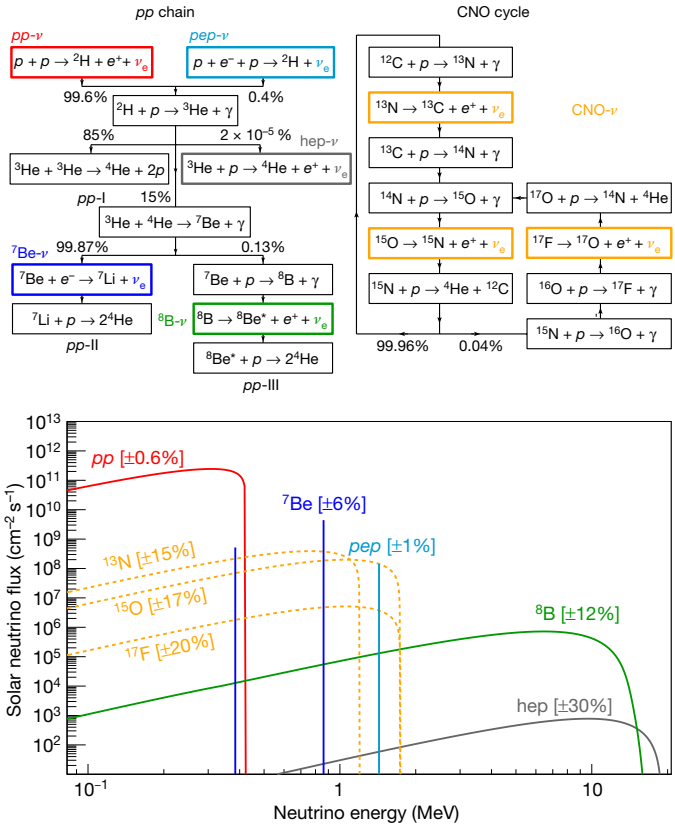

Fig. 1 | Nuclear fusion sequences and neutrino energy spectrum. Schematic view of the *pp* and CNO nuclear fusion sequences. The solar-neutrino energy spectrum is obtained from http://www.sns.ias.edu/~jnb/, using the updated fluxes taken from ref. [18]. The flux (vertical scale) is given in units of $cm^{-2}\ s^{-1}\ MeV^{-1}$ for continuum sources and in $cm^{-2}\ s^{-1}$ for monoenergetic sources.

ranging from less than one to a few tens of counts per day per 100 tons (t) for different solar-neutrino components. To cope with such a low event rate, Borexino has a large target mass (about 300 t) and is housed deep underground, under 3,800 m water equivalent of dolomitic rock that suppresses the flux of cosmic radiation by a factor of approximately one million. For more details on the detector, see Methods.

Radioactive decays of unstable isotopes contained in the scintillator or in the materials surrounding it represent the main sources of background (referred to as internal and external, respectively). Whereas external background is greatly reduced by concentric layers of high-purity materials surrounding the scintillator and by the selection of a centrally located software-defined fiducial volume, most of the internal background can only be cut down by means of liquid-scintillator purification. Particularly, interactions of beta particles (β; electrons and positrons) and of gamma particles (γ; high-energy photons) must be reduced to very low levels, since they cannot be distinguished from neutrino interactions on an event-by-event basis. Borexino has reached unprecedented levels of scintillator radio-purity. As an example, one gram of liquid scintillator contains less than 9.4×10^{-20} grams of uranium-238 and less than 5.7×10^{-19} grams of thorium-232 (95% confidence level, C.L.), a concentration about ten orders of magnitude smaller than in any natural material on Earth. This low level of background has enabled real-time detection of solar neutrinos with an energy threshold of 0.19 MeV, and allowed us to perform the complete spectroscopy of the *pp* chain.

Solar neutrinos reach the Earth as a mixture of all neutrino flavours (electronic, muonic, and tauonic) owing to the flavour-conversion mechanism enhanced by the MSW effect (see Methods). Borexino detects them by means of their weak elastic scattering off electrons. A fraction of the incoming neutrino energy E_ν is transferred to one electron, which deposits it in the liquid scintillator. The scintillator light is detected by about 2,000 photomultiplier tubes, which ensure high detection efficiency of photoelectrons produced by incident optical photons at their photocathodes. For ^{7}Be ($E_\nu = 0.384$ MeV and 0.862 MeV) and *pep* ($E_\nu = 1.44$ MeV) neutrinos, the induced electron recoil endpoints are 0.230 MeV, 0.665 MeV and 1.22 MeV, respectively. For the continuous *pp* and ^{8}B spectra, they are 0.261 MeV and 15.2 MeV, respectively.

The detected light and its time distribution among photomultiplier tubes yield three important quantities for each interaction event in the detector: its deposited energy, roughly proportional to the total number of detected photoelectrons; its position within the detector, obtained from the analysis of the photon arrival times at each photomultiplier tube; and its particle identification, based on a pulse-shape discrimination method that exploits the different time structure of liquid-scintillator light pulses produced by different particles (electrons, positrons, α particles and protons)[27]. For reference, a 1-MeV electron produces on average 500 photoelectrons in 2,000 photomultiplier tubes, its energy is measured with $\sigma \approx 50$ keV and its position is reconstructed[28,29] with $\sigma \approx 12$ cm.

We divided the analysis into two energy regions that are affected by different backgrounds, which need to be handled differently: a low-energy region (LER) of 0.19–2.93 MeV, to measure the *pp*, ^{7}Be and *pep* neutrino interaction rates, and a high-energy region (HER) of 3.2–16 MeV, to measure ^{8}B neutrinos. For the same reason, the HER is further divided into two subregions, below and above 5.7 MeV (HER-I and HER-II). The measurement of ^{8}B neutrinos cannot be extended below 3.2 MeV because of the 2.614-MeV γ-ray background from ^{208}Tl decays, originating from trace ^{232}Th contamination of the thin nylon liquid-scintillator containment vessel.

The reconstructed position of each event within the detector allows us to define a fiducial volume optimized differently for the analysis in the LER and HER-I/II. The LER fiducial volume is chosen to suppress external γ-rays from ^{40}K, ^{214}Bi and ^{208}Tl contained in materials surrounding the scintillator and consists of the innermost 71.3 t of scintillator selected with a radial cut (radius $R < 2.8$ m) and a cut in the vertical direction (-1.8 m $< z < 2.2$ m). The HER is above the energy of the aforementioned γ-rays. The analysis in HER-I requires only a $z < 2.5$ m cut to suppress background events related to a small pinhole in the inner vessel that causes liquid scintillator to leak into the region outside the inner vessel. The total selected mass in this case is 227.8 t. In contrast, the analysis in HER-II uses the entire scintillator volume, 266 t, since the above-mentioned background does not affect this energy window.

The LER analysis uses exclusively Borexino Phase-II data collected between December 2011 and May 2016, in which the internal ^{85}Kr and ^{210}Bi contamination was reduced with respect to Borexino Phase-I, thanks to a liquid-scintillator purification campaign carried out in 2010 and 2011. The total LER exposure is 1,291.51 days × 71.3 t. With the exception of ^{208}Tl decays (Q-value, total energy released in the decay, about 5 MeV), the HER is above the natural, long-lived radioactive background, making it possible to use a larger dataset, collected between January 2008 and December 2016, for a total exposure of 2,062.4 days × 227.8 (266.0) t for HER-I (or HER-II), respectively.

The analysis proceeds in two steps: (1) the event selection, with a different set of cuts in the three energy regions to maximize the signal-to-background ratio, and (2) the extraction of the neutrino and residual background rates with a combined fit of distributions of global quantities built for the events surviving the cuts. The main event selection criteria are conceptually similar for the LER and the HER and are conceived to: reject cosmic muons surviving the mountain shield[30]; reduce the cosmogenic background (that is, radioactive elements produced in muon-induced nuclear spallation processes); and select an optimal spatial region of the scintillator (the fiducial volume). More details on the cuts are discussed in Methods.

Several backgrounds, listed in Table 1 and described in detail in Methods, survive the event selection cuts. To disentangle the neutrino signal from these backgrounds, two different fitting strategies are adopted for the LER and the HER. The LER analysis follows a

Table 1 | Rates of residual backgrounds

Background LER	**Rate (Bq per 100 t)**
^{14}C(0.156 MeV, β^-)	[40.0 ± 2.0]
Background LER	**Rate (counts per day per 100 t)**
^{85}Kr (0.687 MeV, β^-) (internal)	6.8 ± 1.8
^{210}Bi (1.16 MeV, β^-) (internal)	17.5 ± 1.9
^{11}C (1.02–1.98 MeV, β^+) (internal)	26.8 ± 0.2
^{210}Po (5.3 MeV, α) (internal)	260.0 ± 3.0
^{40}K (1.460 MeV, γ) (external)	1.0 ± 0.6
^{214}Bi (<1.764 MeV, γ) (external)	1.9 ± 0.3
^{208}Tl (2.614 MeV, γ) (external)	3.3 ± 0.1
Background HER-I	**Rate (counts per day per 227.8 t)**
μ, cosmogenics, ^{214}Bi (internal)	$[6.1^{+8.7}_{-3.1} \times 10^{-3}]$
(α, n) (external)	0.224 ± 0.078
^{208}Tl(5.0 MeV, β^-, γ) (internal)	[0.042 ± 0.008]
^{208}Tl(5.0 MeV, β^-, γ) (emanated)	0.469 ± 0.063
^{208}Tl(5.0 MeV, β^-, γ) (surface)	1.090 ± 0.046
Background HER-II	**Rate (counts per day per 266.0 t)**
μ, cosmogenics (internal)	$[3.8^{+14.6}_{-0.1} \times 10^{-3}]$
(α, n) (external)	0.239 ± 0.022

Residual background is due to β^- (electrons), β^+ (positrons), γ (gammas), μ (muons), α (alpha particles) and n (neutrons). The background rates are obtained by the fit to the energy spectrum of collected events in the three energy regions used in this study (LER, HER-I and HER-II). We report in parentheses the Q-value and type of particle for each background. The rates in square brackets are estimated independently and are constrained in the fit. Background can be internal (that is, due to events uniformly distributed in the scintillator volume) or external (that is, due to events from sources surrounding the scintillator).

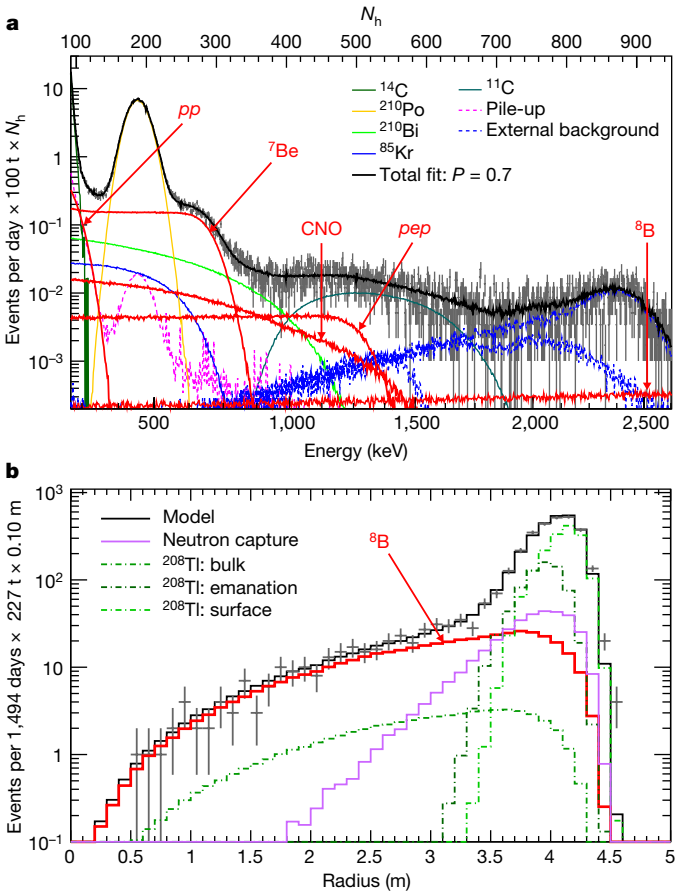

Fig. 2 | Results of the fit used to extract the neutrino signal. Distributions of events after selection cuts and corresponding fits with neutrino and background components. **a**, TFC-subtracted energy spectrum with suppressed ^{11}C background in LER. The horizontal upper scale is in units of N_h, that is, the total number of photons collected for each event. **b**, Radial distribution of events in HER-I.

multivariate approach, simultaneously fitting the energy spectrum, the spatial and the pulse-shape estimator distributions. In the HER-I and HER-II, a fit of the radial distribution of events is performed to separate the ^{8}B neutrino signal (uniformly distributed in the scintillator) from the external background.

Some residual background rates are measured independently, whenever possible, and are constrained in the fit (values between squared brackets in Table 1). The remaining background rates are left free to vary and are returned by the fit together with the neutrino rates.

The results of the fit are exemplified in Fig. 2a, which shows the energy spectrum in the LER after applying the threefold coincidence method (TFC) to reduce the ^{11}C cosmogenic background (see Methods); Fig. 2b shows the radial distribution of the events in HER-I. The different contributions from signal and background as determined by the fit are superimposed to data in the plots. The results of the fit for the untagged backgrounds are summarized in Table 1.

Results

The high-precision solar-neutrino results obtained in this work are summarized in Table 2. The second column reports the measured rates. In the third column, we translate these measurements into the corresponding solar-neutrino fluxes using the known electron and μ/τ neutrino cross-sections[27] and the flavour composition calculated according to the MSW-LMA paradigm (mass and mixing parameters from ref. [19]). The fourth column shows the theoretical fluxes predicted by the SSM under the HZ and LZ assumptions[18].

In the LER multivariate fit, performed to extract the *pp*, *pep* and ^{7}Be neutrino rates, we first constrain the CNO neutrino interaction rate to the value predicted by the HZ-SSM assuming the MSW-LMA scenario (4.92 ± 0.55 counts per day per 100 t)[18,19], then, separately, to the LZ-SSM predictions (3.52 ± 0.37 counts per day per 100 t). Only the *pep* neutrino rate is slightly influenced by this constraint and thus two results for it are reported. In both cases, the absence of the *pep* reaction in the Sun is rejected with $>5\sigma$ significance, enough to definitively claim discovery of solar *pep* neutrinos. The contribution of ^{8}B neutrinos in the LER is very small and its rate was constrained to the value obtained from the HER analysis. Statistical uncertainties are evaluated by profiling the likelihood using Wilks's approximation, whose adequacy in this case is confirmed by Monte Carlo simulations. The ^{7}Be solar-neutrino flux is determined with a total uncertainty of 2.7%, a factor of 1.8 improvement with respect to our previous result[22] and a factor of two smaller than the theoretical uncertainty. The *pp* interaction rate is consistent with our previous result[25] and has an uncertainty of 9.5%. Fits were performed with several hundred configurations, yielding results whose spread is incorporated in the systematic uncertainties (see Methods for more details).

The ^{8}B solar-neutrino flux derived from our measured rate in the entire HER is $(5.68^{+0.39+0.03}_{-0.41-0.03}) \times 10^6$ cm^{-2} s^{-1}, consistent with our previous result[24] and with the high-precision determination by SuperKamiokande[31] and SNO[32]. The equivalent-flavour stable ^{8}B flux, that is, the flux obtained attributing the measured rate entirely to electron neutrinos, is $(2.57^{+0.17+0.07}_{-0.18-0.07}) \times 10^6$ cm^{-2} s^{-1}. The uncertainty in the ^{8}B rate determination is 8%, a more than twofold improvement on our previous measurement[24].

The similarity between the electron recoil spectrum induced by CNO neutrinos and the ^{210}Bi β-decay spectrum makes it impossible to disentangle the two contributions with the spectral fit. For this reason, we only provide an upper limit on the CNO neutrino interaction rate. To do so, we also place an indirect constraint on *pep* neutrinos by exploiting the theoretically well known *pp* and *pep* flux ratio. Using values predicted by the HZ-SSM[18] and including the effect of MSW-LMA oscillations[19], the ratio of *pp* and *pep* neutrino interaction rates is 47.8 ± 0.8. Using the ratio predicted by the LZ-SSM, 47.5 ± 0.8, yields

Table 2 | Borexino experimental solar-neutrino results

Solar neutrino	Rate (counts per day per 100 t)	Flux ($cm^{-2}\,s^{-1}$)	Flux–SSM predictions ($cm^{-2}\,s^{-1}$)
pp	$134 \pm 10^{+6}_{-10}$	$(6.1 \pm 0.5^{+0.3}_{-0.5}) \times 10^{10}$	$5.98(1.0 \pm 0.006) \times 10^{10}$ (HZ) $6.03(1.0 \pm 0.005) \times 10^{10}$ (LZ)
^{7}Be	$48.3 \pm 1.1^{+0.4}_{-0.7}$	$(4.99 \pm 0.11^{+0.06}_{-0.08}) \times 10^{9}$	$4.93(1.0 \pm 0.06) \times 10^{9}$ (HZ) $4.50(1.0 \pm 0.06) \times 10^{9}$ (LZ)
pep (HZ)	$2.43 \pm 0.36^{+0.15}_{-0.22}$	$(1.27 \pm 0.19^{+0.08}_{-0.12}) \times 10^{8}$	$1.44(1.0 \pm 0.01) \times 10^{8}$ (HZ) $1.46(1.0 \pm 0.009) \times 10^{8}$ (LZ)
pep (LZ)	$2.65 \pm 0.36^{+0.15}_{-0.24}$	$(1.39 \pm 0.19^{+0.08}_{-0.13}) \times 10^{8}$	$1.44(1.0 \pm 0.01) \times 10^{8}$ (HZ) $1.46(1.0 \pm 0.009) \times 10^{8}$ (LZ)
$^{8}B_{HER\text{-}I}$	$0.136^{+0.013+0.003}_{-0.013-0.003}$	$(5.77^{+0.56+0.15}_{-0.56-0.15}) \times 10^{6}$	$5.46(1.0 \pm 0.12) \times 10^{6}$ (HZ) $4.50(1.0 \pm 0.12) \times 10^{6}$ (LZ)
$^{8}B_{HER\text{-}II}$	$0.087^{+0.080+0.005}_{-0.010-0.005}$	$(5.56^{+0.52+0.33}_{-0.64-0.33}) \times 10^{6}$	$5.46(1.0 \pm 0.12) \times 10^{6}$ (HZ) $4.50(1.0 \pm 0.12) \times 10^{6}$ (LZ)
$^{8}B_{HER}$	$0.223^{+0.015+0.006}_{-0.016-0.006}$	$(5.68^{+0.39+0.03}_{-0.41-0.03}) \times 10^{6}$	$5.46(1.0 \pm 0.12) \times 10^{6}$ (HZ) $4.50(1.0 \pm 0.12) \times 10^{6}$ (LZ)
CNO	<8.1 (95% C.L.)	$<7.9 \times 10^{8}$ (95% C.L.)	$4.88(1.0 \pm 0.11) \times 10^{8}$ (HZ) $3.51(1.0 \pm 0.10) \times 10^{8}$ (LZ)
hep	<0.002 (90% C.L.)	$<2.2 \times 10^{5}$ (90% C.L.)	$7.98(1.0 \pm 0.30) \times 10^{3}$ (HZ) $8.25(1.0 \pm 0.12) \times 10^{3}$ (LZ)

Measured neutrino rates (second column): for *pp*, ^{7}Be, *pep* and CNO neutrinos we quote the total counts without any threshold; for ^{8}B and hep neutrinos we quote the counts above the corresponding analysis threshold. Neutrino fluxes (third column) are obtained from the measured rates assuming the MSW-LMA oscillation parameters[19], standard neutrino–electron cross-sections[27] and a density of electrons in the scintillator of $(3.307 \pm 0.003) \times 10^{31}$ electrons per 100 t. All fluxes are integral values without any threshold. The result for *pep* neutrinos depends on whether we assume HZ or LZ SSM predictions to constrain the CNO neutrino flux. The last column shows the fluxes predicted by the SSM for the HZ or LZ hypotheses[18].

identical results. We obtain an upper limit of <8.1 counts per day per 100 t (95% C.L.) for the CNO neutrino interaction rate, in agreement with the Borexino sensitivity to CNO studied with Monte Carlo.

For completeness, we also perform a search for the hep neutrinos, emitted by the proton capture reaction of ^{3}He (Fig. 1). The expected flux is more than two orders of magnitude smaller than that of ^{8}B neutrinos. Despite their higher end-point energy, this signal in Borexino is extremely small and covered by background, particularly cosmogenic ^{11}Be decays ($Q = 11.5$ MeV, β^{-}, $\tau = 19.9$ s) and ^{8}B neutrinos. We perform a dedicated analysis on the whole dataset (0.8 kt yr) and in the energy region 11–20 MeV we find 10 ± 3 events, consistent with the expected background. We obtain an upper limit for the hep neutrino flux of $2.2 \times 10^{5}\,cm^{-2}\,s^{-1}$ (90% C.L.) to be compared with the expected flux $7.98 \times 10^{3}\,cm^{-2}\,s^{-1}$ ($8.25 \times 10^{3}\,cm^{-2}\,s^{-1}$) assuming the HZ (LZ) SSM.

Discussion and outlook

The measurements reported in this work represent a complete study of the solar *pp* chain and of its different terminations by means of neutrino detection in a single detector and with a uniform data analysis procedure. These measurements can be used either to test the MSW-LMA paradigm assuming SSM flux predictions or, alternatively, to probe our understanding of solar physics assuming the validity of the neutrino oscillation mechanism.

The interaction rates of *pp*, ^{7}Be, *pep* and ^{8}B neutrinos reported in Table 2 can be used to infer the electron neutrino survival probability at different energies. Assuming the HZ-SSM fluxes[18] and standard neutrino-electron cross-sections[27], we obtain the electron neutrino survival probabilities for each solar-neutrino component: $P_{ee}(pp, 0.267\ \text{MeV}) = 0.57 \pm 0.09$, $P_{ee}(^{7}\text{Be}, 0.862\ \text{MeV}) = 0.53 \pm 0.05$, and $P_{ee}(pep, 1.44\ \text{MeV}) = 0.43 \pm 0.11$. The quoted errors include the uncertainties on the SSM solar-neutrino flux predictions. The ^{8}B electron neutrino survival probability is calculated in each HER range following the procedure described in ref. [24]. We obtain $P_{ee}(^{8}\text{B}_{\text{HER}}, 8.1\ \text{MeV}) = 0.37 \pm 0.08$, $P_{ee}(^{8}\text{B}_{\text{HER-I}}, 7.4\ \text{MeV}) = 0.39 \pm 0.09$, and $P_{ee}(^{8}\text{B}_{\text{HER-II}}, 9.7\ \text{MeV}) = 0.35 \pm 0.09$. These results are summarized in Fig. 3. For non-monoenergetic components, that is, *pp* and ^{8}B neutrinos, the P_{ee} value is quoted for the average energy of neutrinos that produce scattered electrons in the given energy range.

Borexino provides the most precise measurement of the P_{ee} in the LER, where flavour conversion is vacuum-dominated. At higher energy, where flavour conversion is dominated by matter effects in the Sun, the Borexino results are in agreement with the high-precision measurements performed by SuperKamiokande[31] and SNO[32]. Borexino is the only experiment that can simultaneously test neutrino flavour conversion both in the vacuum and in the matter-dominated regime. We performed a likelihood ratio test to compare our data with the MSW-LMA and the vacuum-LMA predictions (pink and grey bands in Fig. 3, respectively). Our data disfavour the vacuum-LMA hypothesis at 98.2% C.L. (see Methods). Overall, the results are in excellent agreement with the expectations from the MSW-LMA paradigm with the oscillation parameters indicated in ref. [19].

Since solar neutrinos are detected on Earth only about 8 min after being produced, they provide a real-time picture of the core of the Sun. In particular, the neutrino fluxes determined experimentally can be used to derive the total power generated by nuclear reactions in the Sun's core[33]. By using exclusively the new Borexino results reported in

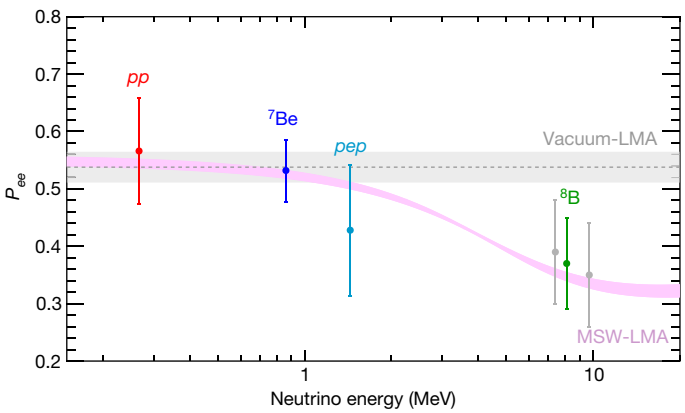

Fig. 3 | Electron neutrino survival probability P_{ee} as a function of neutrino energy. The pink band is the $\pm 1\sigma$ prediction of MSW-LMA with oscillation parameters determined from ref. [19]. The grey band is the vacuum-LMA case with oscillation parameters determined from refs [38,39]. Data points represent the Borexino results for *pp* (red), ^{7}Be (blue), *pep* (cyan) and ^{8}B (green for the HER range, and grey for the separate HER-I and HER-II sub-ranges), assuming HZ-SSM. ^{8}B and *pp* data points are set at the mean energy of neutrinos that produce scattered electrons above the detection threshold. The error bars include experimental and theoretical uncertainties.

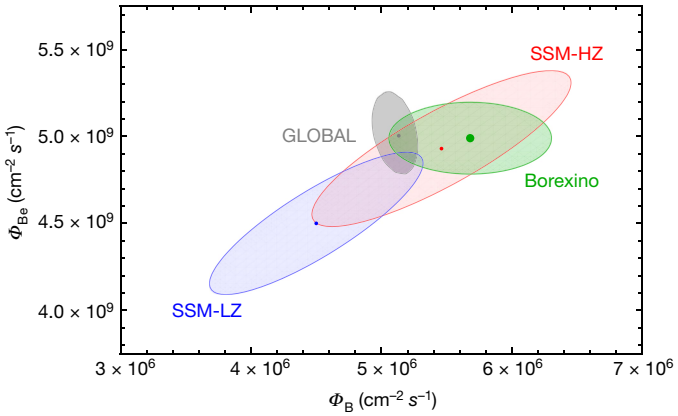

Fig. 4 | Borexino results and analysis in the $\Phi(^7\mathrm{Be})$–$\Phi(^8\mathrm{B})$ space. Borexino results for ^{7}Be and ^{8}B neutrino fluxes (green point and shaded area). Allowed contours in the $\Phi(^7\mathrm{Be})$–$\Phi(^8\mathrm{B})$ space are obtained by combining these new results with all solar and KamLAND data in a global analysis, and leaving free the oscillation parameters θ_{12} and Δm^2_{12} (grey ellipse, marked as GLOBAL). The theoretical prediction for the low-metallicity (LZ) (blue) and the high-metallicity (HZ) (red) Standard Solar Models (SSM)[18] are also shown. The fit returns the following oscillation parameters: $\tan^2\theta_{12} = 0.47 \pm 0.03$ and $\Delta m^2_{12} = (7.5 \times 10^{-5}) \pm 0.03$, in agreement with what is reported in ref. [19] ($\sin^2\theta_{13}$ is fixed to 0.0217; ref. [19]). All contours correspond to 68.27% C.L.

Table 2, we find $L = (3.89^{+0.35}_{-0.42}) \times 10^{33}$ erg s^{-1}, in agreement with the luminosity calculated using the well measured photon output[34,35], $L = (3.846 \pm 0.015) \times 10^{33}$ erg s^{-1}. This confirms experimentally the nuclear origin of the solar power with the best precision obtained by a single solar-neutrino experiment. Considering that it takes around 10^5 years for radiation to flow from the energy-producing region to the surface of the Sun, this comparison proves also that the Sun has been in thermodynamic equilibrium over this timescale.

Furthermore, we derive the ratio $R_{\mathrm{I/II}}$ between the ^{3}He–^{4}He and the ^{3}He–^{3}He fusion rates, which quantifies the relative intensity of the two primary terminations of the *pp* chain (*pp*-II and *pp*-I; see Fig. 1), a critical probe of solar fusion. Neglecting the ^{8}B neutrino contribution, this ratio can be extracted from the measured *pp* and ^{7}Be neutrino fluxes by the relation[36], $R_{\mathrm{I/II}} = 2\Phi(^7\mathrm{Be})/[\Phi(pp) - \Phi(^7\mathrm{Be})]$. We find $R_{\mathrm{I/II}} = 0.178^{+0.027}_{-0.023}$, in agreement with the most up-to-date predicted values of $R_{\mathrm{I/II}} = 0.180 \pm 0.011$ (HZ) and 0.161 ± 0.010 (LZ)[18].

Finally, the Borexino measurements can be used to test the predictions of SSMs with different metallicity. Indeed, the assumed metallicity determines the opacity of solar plasma and, as a consequence, regulates the central temperature of the Sun and the branching ratios of the different *pp*-chain terminations. To perform this test, we use only the results for ^{7}Be and ^{8}B neutrinos, whose fluxes are very different in the HZ- and the LZ-SSM theoretical predictions (differences of 9% and 18%, respectively). Figure 4 shows the results of Borexino (green-shaded ellipse), together with the predictions for the HZ- and LZ-SSMs[18] (red- and blue-shaded ellipses, respectively). Note that the errors in the Borexino measurements are in both cases smaller than the theoretical uncertainties. The theoretical error budget is dominated by uncertainties on the astrophysical factor S_{34} of the $^3\mathrm{He} + {}^4\mathrm{He}$ reaction, on the opacity of the Sun, and on the astrophysical factor S_{17} of the $p + {}^7$Be reaction as discussed in ref. [18].

The Borexino results are compatible with the temperature profiles predicted by both HZ- and LZ-SSMs. However, the ^{7}Be and ^{8}B solar-neutrino fluxes measured by Borexino provide an interesting hint in favour of the HZ-SSM prediction. A frequentist hypothesis test based on a likelihood-ratio test statistics (HZ versus LZ) was performed by computing the probability distribution functions with a Monte Carlo approach. Assuming HZ to be true, our data disfavour LZ at 96.6% C.L. This constraint is slightly stronger than our sensitivity (the median sensitivity is at 94.2% C.L.). A Bayesian hypothesis test[37] yields a Bayes factor of 4.9, confirming a mild preference for HZ (see Methods for more details on both the frequentist and Bayesian studies).

For the sake of completeness, we performed a global fit including the results presented in this work together with all the other solar + KamLAND data. Following the procedure described in ref. [27], we leave the oscillation parameters θ_{12}, Δm^2_{12} and the ^{7}Be and ^{8}B neutrino fluxes free to vary in the fit. Figure 4 shows the allowed regions in the $\Phi(^7\mathrm{Be})$–$\Phi(^8\mathrm{B})$ space determined from this global analysis. The oscillation parameters returned by the fit are consistent with the ones obtained in ref. [19]. It is clear from the output of this global fit that when the Borexino results are combined with those of all other solar-neutrino experiments, the small hint towards HZ further weakens.

In summary, we have reported simultaneous measurements of solar neutrinos from all the reactions belonging to the *pp* nuclear fusion chain. This study confirms the nuclear origin of the solar power and provides the most complete real-time insight into the core of our Sun so far.

1. Atkinson, R. & Houtermans, F. Zur Frage der Aufbaumöglichkeit der Elemente in Sternen. *Z. Phys.* **54**, 656 (1929).
2. von Weizsäcker, C. F. Über Elementumwandlungen im Innern der Sterne I. *Phys. Z.* **38**, 176 (1937).
3. Bethe, H. A. & Critchfield, C. L. The formation of deuterons by proton combination. *Phys. Rev.* **54**, 248 (1938).
4. Bethe, H. Energy production in stars. *Phys. Rev.* **55**, 434 (1939).
5. Bahcall, J. N. *How the Sun Shines*. https://www.nobelprize.org/nobel_prizes/themes/physics/fusion/ (Nobel Media, Stockholm, 2000).
6. Fowler, W. Experimental and theoretical nuclear astrophysics; the quest for the origin of the elements: Nobel prize lecture. *Rev. Mod. Phys.* **56**, 149 (1984).
7. Davis, R. Nobel lecture: a half-century with solar neutrinos. *Rev. Mod. Phys.* **75**, 985 (2003).
8. Abdurashitov, J. et al. Results from SAGE (the Russian-American gallium solar neutrino experiment). *Phys. Lett. B* **328**, 234 (1994).
9. Anselmann, P. et al. Solar neutrinos observed by GALLEX at Gran Sasso. *Phys. Lett. B* **285**, 376 (1992).
10. Hirata, K. et al. Observation of ^{8}B solar neutrinos in the Kamiokande-II detector. *Phys. Rev. Lett.* **63**, 16 (1989).
11. Ahmad, Q. et al. Direct evidence for neutrino flavor transformation from neutral-current interactions in the Sudbury Neutrino Observatory. *Phys. Rev. Lett.* **89**, 011301 (2002).
12. Pontecorvo, B. Neutrino experiments and the problem of conservation of leptonic charge. *Zh. Eksp. Teor. Fiz.* **53**, 1717 (1967).
13. Wolfenstein, L. Neutrino oscillations in matter. *Phys. Rev. D* **17**, 2369 (1978).
14. Mikheyev, S. & Smirnov, A. Resonant amplification of neutrino oscillations in matter and spectroscopy of solar neutrinos. *Sov. J. Nucl. Phys.* **42**, 913 (1985).
15. Bahcall, J. & Davis, R. The evolution of neutrino astronomy. *Publ. Astron. Soc. Pacif.* **112**, 429 (2000).
16. Haxton, W., Hamish Robertson, R. & Serenelli, A. Solar neutrinos: status and prospects. *Annu. Rev. Astron. Astrophys.* **51**, 21 (2013).
17. Bahcall, J. N. *Neutrino Astrophysics* (Cambridge Univ. Press, Cambridge, 1989).
18. Vinyoles, N. et al. A new generation of standard solar models. *Astrophys. J.* **835**, 202 (2017).
19. Esteban, I. et al. Updated fit to three neutrino mixing: exploring the accelerator-reactor complementarity. *J. High Energy Phys.* **1701**, 087 (2017).
20. Arpesella, C. et al. First real time detection of ^{7}Be solar neutrinos by Borexino. *Phys. Lett. B* **658**, 101 (2008).
21. Arpesella, C. et al. Direct measurement of the ^{7}Be solar neutrino flux with 192 days of Borexino data. *Phys. Rev. Lett.* **101**, 091302 (2008).
22. Bellini, G. et al. Precision measurement of the ^{7}Be solar neutrino interaction rate in Borexino. *Phys. Rev. Lett.* **107**, 141302 (2011).
23. Bellini, G. et al. First evidence of *pep* solar neutrinos by direct detection in Borexino. *Phys. Rev. Lett.* **108**, 051302 (2012).
24. Bellini, G. et al. Measurement of the solar ^{8}B neutrino rate with a liquid scintillator target and 3 MeV energy threshold in the Borexino detector. *Phys. Rev. D* **82**, 033006 (2010).
25. Borexino Collaboration. Neutrinos from the primary proton-proton fusion process in the Sun. *Nature* **512**, 383 (2014).
26. Alimonti, G. et al. The Borexino detector at the Laboratori Nazionali del Gran Sasso. *Nucl. Instrum. Meth. A* **600**, 568 (2009).
27. Bellini, G. et al. Final results of Borexino Phase I on low-energy solar neutrino spectroscopy. *Phys. Rev. D* **89**, 112007 (2014).
28. Back, H. et al. Borexino calibrations: hardware, methods and results. *J. Instrum.* **7**, P10018 (2012).

29. Agostini, M. et al. The Monte Carlo simulation of the Borexino detector. *Astropart. Phys.* **97**, 136 (2018).
30. Bellini, G. et al. Muon and cosmogenic neutron detection in Borexino. *J. Instrum.* **6**, P05005 (2012).
31. Abe, K. et al. Solar neutrino measurements in Super-Kamiokande-IV. *Phys. Rev. D* **94**, 052010 (2016).
32. Aharmim, B. et al. Combined analysis of all three phases of solar neutrino data from the Sudbury Neutrino Observatory. *Phys. Rev. C* **88**, 025501 (2013).
33. Bergström, J. et al. Updated determination of the solar neutrino fluxes from solar neutrino data. *J. High Energy Phys.* **2016**, 132 (2016).
34. Chapman, G. A. in *Encyclopedia of Planetary Science and Encyclopedia of Earth Science* 748 (Springer, 1997).
35. Fröhlich, C. & Lean, J. The Sun's total irradiance: cycles, trends and related climate change uncertainties since 1976. *Geophys. Res. Lett.* **25**, 4377 (1998).
36. Bahcall, J. & Pena-Garay, C. A road map to solar neutrino fluxes, neutrino oscillation parameters and tests for new physics. *J. High Energy Phys.* **2003**, 4 (2003).
37. Caldwell, A., Kollar, D., Kroninger, K. BAT—the Bayesian Analysis Toolkit. *Comput. Phys. Commun.* **180**, 2197 (2009).
38. Feng Pen An et al. Measurement of electron antineutrinon oscillation based on 1230 days of operation of the Daya Bay experiment. *Phys. Rev. D* **95**, 072006 (2017).
39. Gando, A. et al. Reactor on-off antineutrino measurement with KamLAND. *Phys. Rev. D* **88**, 033001 (2013).

Acknowledgements The Borexino programme is made possible by funding from INFN (Italy), NSF (USA), BMBF, DFG, HGF and MPG (Germany), RFBR (grants 16-29-13014ofi-m and 17-02-00305A), RSF (grant 17-12-01009) (Russia), and NCN (grant number UMO 2017/26/M/ST2/00915) (Poland). We acknowledge also the computing services of the Bologna INFN-CNAF data centre and LNGS Computing and Network Service (Italy), of Jülich Supercomputing Centre at FZJ (Germany), and of ACK Cyfronet AGH Cracow (Poland). We acknowledge the hospitality and support of the Laboratori Nazionali del Gran Sasso (Italy).

Reviewer information *Nature* thanks A. Serenelli and the other anonymous reviewer(s) for their contribution to the peer review of this work.

Author contributions The Borexino detector was designed, constructed, and commissioned by the Borexino Collaboration over the span of more than 15 years. The Borexino Collaboration sets the science goals. Scintillator purification and handling, source calibration campaigns, photomultiplier tube and electronics operations, signal processing and data acquisition, Monte Carlo simulations of the detector, and data analyses were performed by Borexino members, who also discussed and approved the scientific results. This manuscript was prepared by a subgroup of authors appointed by the Collaboration and subjected to an internal collaboration-wide review process. All authors reviewed and approved the final version of the manuscript.

Competing interests The authors declare no competing interests.

The Borexino Collaboration

M. Agostini[1], K. Altenmüller[1], S. Appel[1], V. Atroshchenko[2], Z. Bagdasarian[3], D. Basilico[4], G. Bellini[4], J. Benziger[5], D. Bick[6], G. Bonfini[7], D. Bravo[4,29], B. Caccianiga[4]*, F. Calaprice[8], A. Caminata[9], S. Caprioli[4], M. Carlini[7], P. Cavalcante[7,10], A. Chepurnov[11], K. Choi[12], L. Collica[4], D. D'Angelo[4], S. Davini[9], A. Derbin[13], X. F. Ding[7,14], A. Di Ludovico[8], L. Di Noto[9], I. Drachnev[13], K. Fomenko[15], A. Formozov[4,11,15], D. Franco[16], F. Gabriele[7], C. Galbiati[8,14], C. Ghiano[7], M. Giammarchi[4], A. Goretti[7], M. Gromov[11], D. Guffanti[7,14], C. Hagner[6], T. Houdy[16], E. Hungerford[17], Aldo Ianni[7,18], Andrea Ianni[8], A. Jany[19], D. Jeschke[1], V. Kobychev[20], D. Korablev[15], G. Korga[17], D. Kryn[16], M. Laubenstein[7], E. Litvinovich[2,21], F. Lombardi[7,30], P. Lombardi[4], L. Ludhova[3,22], G. Lukyanchenko[2], L. Lukyanchenko[2], I. Machulin[2,21], G. Manuzio[9], S. Marcocci[7,14,31], J. Martyn[23], E. Meroni[4], M. Meyer[24], L. Miramonti[4], M. Misiaszek[19], V. Muratova[13], B. Neumair[1], L. Oberauer[1], B. Opitz[6], V. Orekhov[2], F. Ortica[25], M. Pallavicini[9], L. Papp[1], Ö. Penek[3,22], N. Pilipenko[13], A. Pocar[26], A. Porcelli[23], G. Raikov[2], G. Ranucci[4], A. Razeto[7], A. Re[4], M. Redchuk[3,22], A. Romani[25], R. Roncin[7,16], N. Rossi[7,32], S. Schönert[1], D. Semenov[13], M. Skorokhvatov[2,21], O. Smirnov[15], A. Sotnikov[15], L. F. F. Stokes[7], Y. Suvorov[2,27,33], R. Tartaglia[7], G. Testera[9], J. Thurn[24], M. Toropova[2], E. Unzhakov[13], F. L. Villante[7,28], A. Vishneva[15], R. B. Vogelaar[10], F. von Feilitzsch[1], H. Wang[27], S. Weinz[23], M. Wojcik[19], M. Wurm[23], Z. Yokley[10], O. Zaimidoroga[15], S. Zavatarelli[9], K. Zuber[24] & G. Zuzel[19]

[1]Physik-Department and Excellence Cluster Universe, Technische Universität München, Garching, Germany. [2]National Research Centre Kurchatov Institute, Moscow, Russia. [3]Institut für Kernphysik, Forschungszentrum Jülich, Jülich, Germany. [4]Dipartimento di Fisica, Università degli Studi e INFN, Milano, Italy. [5]Chemical Engineering Department, Princeton University, Princeton, NJ, USA. [6]Institut für Experimentalphysik, Universität Hamburg, Hamburg, Germany. [7]INFN, Laboratori Nazionali del Gran Sasso, Assergi, Italy. [8]Physics Department, Princeton University, Princeton, NJ, USA. [9]Dipartimento di Fisica, Università degli Studi e INFN, Genova, Italy. [10]Physics Department, Virginia Polytechnic Institute and State University, Blacksburg, VA, USA. [11]Lomonosov Moscow State University Skobeltsyn Institute of Nuclear Physics, Moscow, Russia. [12]Department of Physics and Astronomy, University of Hawaii, Honolulu, HI, USA. [13]St Petersburg Nuclear Physics Institute, NRC Kurchatov Institute, Gatchina, Russia. [14]Gran Sasso Science Institute, L'Aquila, Italy. [15]Joint Institute for Nuclear Research, Dubna, Russia. [16]AstroParticule et Cosmologie, Univ. Paris Diderot, CNRS/IN2P3, CEA/IRFU, Observatoire de Paris, Sorbonne Paris Cité, Paris, France. [17]Department of Physics, University of Houston, Houston, TX, USA. [18]Laboratorio Subterráneo de Canfranc, Canfranc Estacion Huesca, Spain. [19]M. Smoluchowski Institute of Physics, Jagiellonian University, Krakow, Poland. [20]Kiev Institute for Nuclear Research, Kiev, Ukraine. [21]National Research Nuclear University MEPhI (Moscow Engineering Physics Institute), Moscow, Russia. [22]RWTH Aachen University, Aachen, Germany. [23]Institute of Physics and Excellence Cluster PRISMA, Johannes Gutenberg Universität Mainz, Mainz, Germany. [24]Department of Physics, Technische Universität Dresden, Dresden, Germany. [25]Dipartimento di Chimica, Biologia e Biotecnologie, Università degli Studi e INFN, Perugia, Italy. [26]Amherst Center for Fundamental Interactions and Physics Department, University of Massachusetts, Amherst, MA, USA. [27]Physics and Astronomy Department, University of California Los Angeles (UCLA), Los Angeles, California, USA. [28]Dipartimento di Scienze Fisiche e Chimiche, Università dell'Aquila, L'Aquila, Italy. [29]Present address: Universidad Autónoma de Madrid, Ciudad Universitaria de Cantoblanco, Madrid, Spain. [30]Present address: Physics Department, University of California, San Diego, CA, USA. [31]Present address: Fermi National Accelerator Laboratory (FNAL), Batavia, IL, USA. [32]Present address: Dipartimento di Fisica, Sapienza Università di Roma e INFN, Rome, Italy. [33]Present address: Dipartimento di Fisica, Università degli Studi Federico II e INFN, Naples, Italy. *e-mail: spokesperson-borex@lngs.infn.it

METHODS

The Borexino detector. Borexino is a large liquid-scintillator experiment located deep underground at the Laboratori Nazionali del Gran Sasso in Italy. Borexino is designed to achieve extremely low background conditions. The active core of the detector consists of about 300 t of pseudocumene (1,2,4-trimethylbenzene) doped with 1.5 g per litre of PPO (2,5-diphenyloxazole) and contained in a spherical nylon inner vessel (radius $R = 4.25$ m). The scintillator is surrounded by a non-scintillating pseudocumene-based buffer liquid which serves as a shield against external radioactivity (see Extended Data Fig. 1). The scintillator fluorescence light is collected by 2,212 photomultiplier tubes mounted on the Stainless Steel Sphere (radius $R = 6.9$ m). The entire detector is enclosed in a domed, cylindrical tank filled with high-purity water, equipped with 208 photomultiplier tubes, which provides extra shielding against external radioactivity (photons and neutrons), and also serves as an active water Cherenkov veto against residual cosmic muons. A detailed description of the Borexino detector is found in ref. [26].

The SSM and the solar metallicity controversy. The SSM is a solution of the stellar evolution equations for stars of one solar mass, calibrated to match present-day, measured surface properties of the Sun. A fundamental assumption is that the Sun was initially chemically homogeneous and that during its 4.56-Gyr-long evolution, it has modified its chemical composition solely due to nuclear reactions and elemental diffusion. The model calibration is done by adjusting the mixing length parameter and the initial chemical composition in order to reproduce the observed solar luminosity, radius, and current surface composition. As a result of this procedure, the SSM has no free parameters and completely determines the mechanical and thermal properties of the Sun.

The SSM predicts that most of the solar energy (>99%) is produced by the so-called *pp* chain (see Fig. 1) that fuses hydrogen into ^{4}He: the chain is initiated by the *pp* fusion reaction and, to a minor extent, by the alternative three-body *pep* process. These reactions produce deuterons, which are efficiently converted into ^{3}He by the subsequent deuteron–proton reaction. The *pp* chain mostly terminates with the $^3\mathrm{He} + {}^3\mathrm{He} \rightarrow {}^4\mathrm{He} + 2p$ reaction (*pp*-I termination). In the late 1950s, the cross-section for the competing $^3\mathrm{He} + {}^4\mathrm{He} \rightarrow {}^7\mathrm{Be} + \gamma$ reaction was discovered[40] to be about one thousand times larger than previously thought, causing the branching ratios of the *pp*-II and *pp*-III terminations to be non-negligible. An alternative process is the so-called CNO cycle, a closed-loop nuclear reaction in which ^{12}C, ^{14}N, and ^{16}O nuclei catalyse hydrogen fusion into ^{4}He. The CNO cycle is a subdominant energy-producing mechanism in stars like the Sun or lighter, but is believed to be the dominant fusion mechanism in heavier or older stars.

For each ^{4}He nucleus produced in the Sun, two electron-flavour neutrinos are emitted. Neutrinos free-stream across the solar plasma and reach the Earth travelling close to the speed of light in about 8 min, resulting in a total flux of about $6.5 \times 10^{10}\ \mathrm{cm^{-2}\ s^{-1}}$. The solar-neutrino spectrum depends on the branching ratios of the different *pp* chain terminations and on the relative intensity of the *pp* chain and the CNO cycle. A large percentage (about 90%) of the neutrinos emitted by the Sun are produced in the primary *pp* fusion reaction (producing *pp* neutrinos). Most of the remaining 10% of the solar-neutrino flux is emitted in the electron capture reaction on ^{7}Be (producing ^{7}Be neutrinos), which appears along the *pp*-II branch of the chain. Smaller contributions come from *pep* fusion (the *pep* neutrinos) and from ^{8}B decays in the *pp*-III branch (producing ^{8}B neutrinos). Neutrinos from proton capture of ^{3}He (hep neutrinos) are expected to be emitted with negligible probability (10^{-7}) and are beyond current detection sensitivity. The predicted energy spectrum of all neutrinos emitted along the *pp* chain, including spectral shapes and intensity before neutrino oscillations are shown in Fig. 1.

The predictions of the SSM have been tested by solar-neutrino experiments and by helioseismology (which determines the properties of the solar interior by studying the propagation of seismic waves at the Sun's surface). However, important questions about the Sun still call for an answer. For example, the solar metallicity—the abundance of elements heavier than He—is poorly understood, although it is a fundamental input when constructing SSMs and a relevant parameter in astrophysics, since almost all determinations of elemental abundances in astronomical objects rely upon the solar composition. Recent determinations of the solar surface composition[41–43] suggest that the solar metallicity might be lower than previously assumed[44,45]. SSMs that incorporate these lower abundances, however, agree less well with helioseismic data: this is often referred to as the solar metallicity problem.

Solar-neutrino measurements provide fundamental clues for the solution of this puzzle. Indeed, the opacity of the solar plasma is strongly influenced by the presence of heavy elements. Since opacity determines the efficiency of radiative energy transfer, the metal content of solar matter affects the temperature profile of the Sun. As a consequence, metallicity determines the branching ratios for the various terminations of the *pp* chain, as well as the relative intensity of the *pp* chain with respect to the CNO cycle. A precise determination of the solar-neutrino fluxes comprising both the *pp* chain and the CNO cycle is thus a direct, robust way to settle the solar metallicity controversy. In the main text we compare our experimental results with predictions of HZ and LZ SSMs[18].

Neutrino oscillations and the MSW effect. For many years, the experimental results on solar neutrinos have been at odds with the predictions of the SSM: all the experiments observed a large deficit of neutrinos with respect to expectations. This 30-year-long controversy was settled only in 2002 by the experiment SNO[11], which proved unambiguously that the solution to the 'solar-neutrino problem' was not to be searched for in solar physics, but in neutrino physics, namely, in the quantum mechanics phenomenon of flavour oscillations[12]. Through this mechanism, solar neutrinos, which are born in the Sun as electron neutrinos, ν_e, have a non-zero probability to transform into neutrinos with a different flavour (either ν_μ or ν_τ) during propagation and are therefore less likely to be detected on Earth. For oscillations to occur, two conditions must be met: (1) mass and flavour eigenstates for neutrinos must not coincide, which implies the existence of a non-trivial mixing matrix which transforms one into the other; and (2) the mass of at least one neutrino must be different from 0. The relevant parameters for solar-neutrino oscillations are the mixing angle θ_{12} and the squared mass difference between the mass eigenstates, mostly contributing to ν_e, that is, Δm^2_{12}. The probability of flavour conversion is enhanced when neutrinos cross the dense solar medium, because of coherent forward scattering on electrons. This mechanism is referred to as the Mikheyev–Smirnov–Wolfenstein (MSW) matter effect[13,14] and for the specific values of Δm^2_{12} and of the Sun density profile it fully describes solar neutrinos with energies greater than about 5 MeV. For energies below 1 MeV, the vacuum oscillation mechanism dominates, whereas in the intermediate-energy region, a smooth transition occurs. Figure 3 shows the survival probability P_{ee} for ν_e produced in the Sun as a function of the neutrino energy (pink curve) for the oscillation parameters obtained by a global fit to all solar-neutrino, reactor and accelerator experiments[19]. The values of Δm^2_{12} (about $7.5 \times 10^{-5}\ \mathrm{eV^2}$) and of θ_{12} (about 33°) correspond to the so-called Large Mixing Angle solution (LMA) of the solar-neutrino problem.

Event selection and residual backgrounds. The analysis starts with data selection aimed at reducing the rate of background events. The selection criteria, conceptually similar for the LER and HER, are conceived to: (1) reject cosmic muons penetrating the mountain shield; (2) reduce the cosmogenic background, that is, the decays of short-lived radioactive elements produced in muon-induced nuclear spallation processes in the detector; and (3) select a fiducial volume of the scintillator, optimized separately for the LER and HER-I/II analyses.

Rejection of muons is achieved by combining the external Cherenkov veto information with a pulse shape analysis of the scintillator signals, and displays an overall efficiency[30] of 99.992%. The reduction of cosmogenic background is obtained by excluding events collected during a given time Δt following every muon crossing the scintillator.

For the LER, a short muon veto time $\Delta t = 300$ ms is enough to efficiently suppress most relevant cosmogenic isotopes. An exception is ^{11}C ($Q = 0.96$ MeV, β^+, $\tau = 29.4$ min), which is produced in situ by muon spallation, and has a mean lifetime that greatly exceeds the short muon veto time cut. ^{11}C has a fairly constant concentration in the scintillator (around 30 counts per day per 100 t) determined by the equilibrium between its production and decay rate and cannot be reduced by any purification procedure. It is therefore one of the most important backgrounds and must be treated with a specific analysis (see next paragraph).

For the HER, the rejection of cosmogenic background requires a larger time window of $\Delta t = 6.5$ s to suppress ^{12}B, ^{8}He, ^{9}C, ^{9}Li, ^{8}B, ^{6}He and ^{8}Li decays. Furthermore, for the HER analysis a 2-ms veto is applied after muons that cross the buffer liquid only. This veto aims at rejecting 4.95-MeV γ-rays following the capture of cosmogenic neutrons on ^{12}C nuclei; an additional cut is applied around the capture position of cosmogenic neutrons, when this happens inside the scintillator, to remove ^{10}C ($Q = 3.6$ MeV, β^+, $\tau = 27.8$ s).

Both in the LER and in the HER, ^{214}Bi and ^{214}Po from the ^{238}U natural decay chain are removed by exploiting the space-time correlation of their fast $\beta + \alpha$ delayed coincidence decays.

The analysis in the LER and HER-I/II use different fiducial volumes. The LER fiducial volume focuses on suppressing external γ-rays from ^{40}K, ^{214}Bi and ^{208}Tl contained in materials surrounding the scintillator. It consists of the central 71.3 t of scintillator, selected by applying a radial cut ($R < 2.8$ m) and a cut along the vertical axis ($-1.8\mathrm{m} < z < 2.2$ m). The HER is above the energy of the aforementioned γ-rays. The analysis in HER-I only requires a $z < 2.5$ m cut to suppress background events related to a small pinhole in the nylon vessel that causes scintillating fluid to leak into the region surrounding it. The total HER-I target mass is 227.8 t. The analysis in HER-II uses the entire scintillator volume of 266 t. More details on the selection criteria can be found in refs [24,25,27].

After the selection cuts described above, some residual background remains both in the LER and in the HER. The LER residual background is detailed in Table 1, and is mostly due to traces of radioactive isotopes contaminating the scintillator—that is, ^{14}C, ^{210}Po (either from ^{210}Pb decay or out of equilibrium), ^{85}Kr, ^{210}Bi (from ^{210}Pb) and pile-up of uncorrelated events. A small contribution to the LER rate also comes from external ^{208}Tl, ^{214}Bi and ^{40}K γ-rays emerging from materials surrounding the scintillator. In the LER fit, the ^{14}C rate is

quantified and constrained using an independent sample of events acquired without any trigger threshold[25]. The contribution of pile-up, dominated by simultaneous ^{14}C decays at different detector positions, is treated using the following two methods described in refs [25,29]: in one case, we construct the pile-up spectrum starting from real or Monte Carlo datasets; in the other, we convolve all spectral components with a randomly acquired spectrum (that is, with events acquired with a solicited, external trigger).

The residual backgrounds affecting the HER-I and HER-II are also listed in Table 1. Some of the internal events (that is, events uniformly distributed in the scintillator volume) are due to muons, cosmogenic isotopes, and ^{214}Bi decays surviving the cuts. The total contribution of these backgrounds has been evaluated separately for the HER-I and the HER-II, following the procedure described in ref. [24], and constrained in the fit. In addition, the presence of untagged ^{11}Be ($Q = 11.5$ MeV, β^-, $\tau = 19.9$ s) is estimated by adopting a technique based on a multivariate fit, which includes the energy spectrum and the time profile of events with respect to the preceding muon, and is found to be compatible with zero. The HER-I is also affected by internal ^{208}Tl decays, which come from the residual ^{232}Th contamination of the liquid scintillator. In the fit, this rate is constrained to the value obtained by counting the ^{212}Bi–^{212}Po $\beta + \alpha$ fast delayed coincidences. External ^{208}Tl contamination contributes to the HER-I with two distinct components: one from contamination directly on the inner vessel surface, and another from decays of nuclei that have recoiled off the inner vessel into the liquid scintillator or originated from the volatile progenitor of ^{208}Tl, ^{220}Rn, which has emanated out of the nylon. The rates of both components are left free to vary in the radial fit. Finally, HER-I and HER-II are also polluted by γ-rays following the capture of radiogenic neutrons produced via (α, n) or spontaneous fission reactions of ^{238}U, ^{235}U and ^{232}Th in the Stainless Steel Sphere and photomultiplier tubes. This rate is also a free parameter of the fit.

The ^{11}C background. The ^{11}C background is not removed by the short veto cut after muons. To disentangle its contribution from the neutrino signal, we use the TFC method[23,27], which exploits the time and space correlation between muons, the neutrons they produce in combination with ^{11}C, and the subsequent ^{11}C decays. With this method we divide the events passing the selection cuts in two complementary datasets: one is depleted in ^{11}C (TFC-subtracted) and preserves (64.28 ± 0.01)% of the total exposure; the other contains (92 ± 4)% of the ^{11}C (TFC-tagged). The energy spectra of these two datasets are fitted simultaneously in the multivariate fit (see next paragraph). The residual ^{11}C (positron) background in the TFC-subtracted spectrum is further disentangled from electron-like events by including in the multivariate fit the distribution of a pulse-shape discrimination variable[23,27]. It is in fact observed that the time distribution of scintillation photons slightly differs between electron and positron events, for the following reasons: (1) positron produces ortho-positronium half of the time, which delays the annihilation by around 3 ns (ref. [46]); (2) the positron energy deposition occurs in multiple sites within the detector, owing to the production of annihilation γ-rays. These effects tend to delay and extend the time distribution of the scintillator pulse for positrons with respect to electron events, a handle we exploit for ^{11}C background rejection.

Fitting procedure for extraction of solar-neutrino rates. To disentangle the neutrino signal rates from the residual background, we apply different fitting strategies for the LER and the HER. For LER, we adopt a multivariate approach and simultaneously fit the TFC-subtracted and the TFC-tagged energy spectra, the spatial distribution, and the distribution of the pulse-shape discrimination variable. The spatial distribution is crucial to separate the residual external background component, while the pulse-shape estimator is optimized to separate positrons from electrons, which is key to disentangling ^{11}C from the other fit species (see above). The reference radial distributions for external and internal events used in the multivariate fit are built with a comprehensive Geant4-based Monte Carlo simulation, carefully tuned and validated with calibration data[28,29]. The spectral shapes of signal and background components used in the multivariate fit of the LER are also obtained from simulations. In addition, the fit of the energy spectra is performed using analytical spectral functions[25,27], where the nonlinearity of the energy scale (due, for example, to ionization quenching and Cherenkov light emission) and the spatially non-uniform detector response are included via nuisance parameters, some of which are left free to vary in the fit. The reference positron pulse-shape distribution used in the LER multivariate fit is based on events selected with the TFC method described above, tuned to obtain a nearly pure sample of ^{11}C events. The reference electron pulse-shape distribution is obtained from simulations and checked on data using electron-like events isolated via the ^{214}Bi–^{214}Po coincidences.

In the HER-I and HER-II, the analysis is based on a fit to the radial distribution of the events to separate the ^{8}B neutrino signal (uniformly distributed in the scintillator) from the external background components. Like the LER fit, the reference radial distributions for external and internal events used in the HER fit are built with Geant4-based Monte Carlo simulations. For more details on the fit to extract the neutrino signal see ref. [27].

Systematic uncertainties in the analysis. The detector energy response and uniformity has been carefully studied by means of an extensive calibration campaign which was carried out in 2009[28]. The calibration data were used to tune the input parameters of the Borexino Monte Carlo package, a custom Geant4-based code[47] that can simulate all processes following the interaction of a particle in the detector, including all known characteristics of the apparatus[29]. After tuning, the agreement between Monte Carlo and calibration data is very good for both the LER and the HER: for the energies relevant to the LER analysis, the overall uncertainty is below 1%, while for the HER analysis, it is around 1.9%.

In spite of this remarkable understanding of the detector response throughout the scintillator volume and in a large energy range, an extensive study of possible sources of systematic errors has been performed both for the LER and for the HER. The results of these studies are summarized in Extended Data Tables 1 and 2, respectively.

Concerning the analysis in the LER, the main contribution to the systematic error comes from the fit model, that is, possible residual inaccuracies in the modelling of the detector response (energy scale, uniformity of the energy response, pulse-shape discrimination shape) and uncertainties in the theoretical energy spectra used in the fit. These systematic effects have been estimated by means of a Monte Carlo method: an ensemble of 100,000 datasets are simulated from a family of probability density functions, which includes deformations caused by the inaccuracies under study. The magnitude of the deformations was chosen to be within the range allowed by the available calibration data. These data are then fitted following the same procedure used for real data and differences in the results are quoted as systematics (see first line in Extended Data Table 1).

The second source of systematics is related to the fit method, that is, whether the reference probability density functions used in the fit are entirely derived from Monte Carlo simulations or analytically. Further systematic effects arise from the choice of the energy estimator, from the details of the implementation of the pile-up of uncorrelated events, from using different fit energy ranges and binning, from the inclusion of an independent constraint on ^{85}Kr obtained from its sub-dominant delayed coincidence decay (branching ratio 0.43%), and from the estimation of the target fiducial mass. This last uncertainty is determined with calibration data, by using sources deployed in known positons throughout the detector volume.

Concerning the HER analysis, the most important systematic uncertainties arise from the determination of the target mass, from the energy scale, and from the z-cut applied in the HER-I range (see Extended Data Table 2).

The target mass uncertainty is related to the fact that the amount of scintillator contained in the inner vessel is slowly decreasing (by less than 0.5 m^3 per year), due to a small pinhole in the nylon membrane. We monitor the evolution of the scintillator mass on a week-by-week basis, by studying the inner vessel shape, which is obtained from the spatial distribution of its surface contamination. This method gives an average total mass of 266 t with an error of about 2%.

The impact of the uncertainty of the energy scale on the number of events falling in the HER-I and HER-II energy window has been evaluated with a full Monte Carlo simulation and has been included in the systematic error (see second line of Extended Data Table 2).

As mentioned in the main text, the HER-I analysis requires a cut on the vertical coordinate to remove background events owing to a small pinhole in the nylon vessel that causes the scintillator to leak into the buffer liquid. To estimate possible systematics associated to this cut, the HER-I analysis was performed with a modified z-cut, $\pm$0.5 m around the chosen value (2.5 m). Differences in the results have been included as systematic error.

Frequentist hypothesis test of MSW versus vacuum oscillations. Borexino provides results on the electron neutrino survival probability (P_{ee}) in the entire solar-neutrino energy range. We are therefore able to perform a statistical study to compare the compatibility of our measurement with two different hypotheses: the standard oscillation scenario, MSW-LMA, and the vacuum-LMA scenario, in which matter effects are not present (and which is taken as our null hypothesis).

The survival probability $P_{ee}^{\text{MSW-LMA}}$ in the MSW-LMA scenario depends not only on the oscillation parameters θ_{12}, θ_{13} and Δm^2_{12} valid in vacuum, but also on the neutrino-energy-dependent potential characterizing the interaction of neutrinos with the dense solar core. It can be expressed as follows[48]:

$$P_{ee}^{\text{MSW-LMA}} = \frac{1}{2}\cos^4\theta_{13}\,(1 + \cos 2\theta_{12}^{\text{M}}\cos 2\theta_{12})$$

where

$$\cos 2\theta_{12}^{\text{M}} = \frac{\cos 2\theta_{12} - \beta}{\sqrt{(\cos 2\theta_{12} - \beta)^2 + \sin^2 2\theta_{12}}}$$

and

$$\beta = \frac{2\sqrt{2}\,G_{\text{F}}\cos^2\theta_{13} n_{\text{e}} E_{\nu}}{\Delta m_{12}}$$

where θ^{M} is the mixing angle in matter, G_F is the Fermi coupling constant and n_e is the density of electrons in the matter. Using the current set of oscillation parameters and errors derived in ref. [19], and following the procedure described in ref. [27], we obtain the pink band in Fig. 3.

If matter effects were not present, the survival probability for solar neutrinos would be approximated by the expression P_{ee}^{vacuum}:

$$P_{ee}^{vacuum} = \cos^4\theta_{13}\left(1-\frac{1}{2}\sin^2 2\theta_{12}\right)+\sin^4\theta_{13}$$

which is independent of the neutrino energy E_ν. Taking for θ_{13} and θ_{12} the values and errors measured by reactor neutrino experiments in refs [38,39], the survival probability P_{ee}^{vacuum} as a function of E_ν corresponds to the grey band in Fig. 3.

We performed a frequentist analysis, in which we adopt a test statistics t based on the ratio between the likelihood L obtained assuming MSW-LMA and vacuum-LMA:

$$t = -2\log[L(\mathrm{MSW})/L(\mathrm{vacuum})] = \chi^2(\mathrm{MSW}) - \chi^2(\mathrm{vacuum})$$

The probability distribution of t is built with a Monte Carlo method: we randomly generate thousands of values of P_{ee} in the MSW-LMA hypothesis (by sampling the pink curve in Fig. 3 and including both theoretical and experimental uncertainties) and for each set of data we estimate t and build its distribution (red curve on the left in Extended Data Fig. 2). In the same way, we simulate thousands of P_{ee} values in the vacuum-LMA hypothesis and we build the corresponding t distribution (blue curve on the right in Extended Data Fig. 2).

The actual Borexino results for P_{ee} for *pp*, ^{7}Be, *pep* and ^{8}B gives a value of $t_{BX} = -4.16$ (indicated as a dashed line in Extended Data Fig. 2), which allows us to disfavour the vacuum-LMA hypothesis with a P value of 0.018 (integral of the small tail of the blue curve to the left of t_{BX}), corresponding to a C.L. of 98.2%. For more details on the choice of the test statistics see ref. [49].

Frequentist and Bayesian hypothesis test of the HZ versus LZ models. The combination of the Borexino measurement on ^{8}B and ^{7}Be fluxes provides an interesting hint in favour of the solar temperature profile predicted by the HZ-SSM. This was obtained by performing both a frequentist and a Bayesian hypothesis test.

In the frequentist analysis, we used a test statistics t based on the ratio between the likelihood obtained assuming HZ and LZ:

$$t = -2\log[L(\mathrm{HZ})/L(\mathrm{LZ})] = \chi^2(\mathrm{HZ}) - \chi^2(\mathrm{LZ})$$

The probability distribution of t is built with a Monte Carlo method (full Neumann construction of the confidence intervals): we randomly generate thousands of fake ^{7}Be–^{8}B results in the HZ hypothesis (sampling a distribution that includes both theoretical and experimental errors) and for each set of data we estimate t (red distribution on the left in Extended Data Fig. 3). In the same way, we simulate thousands of fake ^{7}Be–^{8}B results in the LZ hypothesis and we build the corresponding t distribution (in blue on the right in Extended Data Fig. 3).

The value of t corresponding to the actual Borexino result for ^{7}Be–^{8}B is shown in the plot as the dotted line at $t_{BX} = -3.49$, relatively far from the maximum of the LZ probability distribution (blue curve). This allows us to disfavour the LZ hypothesis with a P value of 0.034 (integral of the small tail of the blue curve to the left of t_{BX}), corresponding to a C.L. of 96.6%. The result is slightly better than the median P value expected (0.058), which corresponds to a median significance of 94.2% C.L. For more details on the choice of the test statistics see ref. [49].

In the Bayesian analysis we constructed two models, one for the HZ and the other for the LZ hypothesis, in which the free parameters are the fluxes of ^{8}B and of ^{7}Be. The model predictions are used as prior probability distributions. The likelihood is constructed as the sum of two Gaussian measurements, one for the flux of ^{8}B and the other for the flux of ^{7}Be.

We compare the two models assuming that they have the same probability a priori (50% for the HZ hypothesis and 50% for LZ hypothesis). Like the frequentist analysis, the data show a mild preference for HZ with respect to LZ. The odds are 5:1 or, equivalently, the Bayes factor is 4.9. For more details on the Bayesian method see ref. [37].

Data availability

The datasets generated during the current study are freely available in the repository https://bxopen.lngs.infn.it/. Additional information is available from the Borexino Collaboration spokesperson (spokesperson-borex@lngs.infn.it) upon reasonable request.

40. Holmgren, H. & Johnston, R. $He^3(\alpha,\gamma)Li^7$ and $He^3(\alpha,\gamma)Be^7$ reactions. *Phys. Rev.* **113**, 1556 (1959).
41. Asplund, M., Grevesse, N., Sauval, A. J. & Scott, P. The chemical composition of the Sun. *Annu. Rev. Astron. Astrophys.* **47**, 481 (2009).
42. Caffau, E., Ludwig, H. G., Steffen, M., Freytag, B. & Bonifacio, P. Solar chemical abundances determined with a CO5BOLD 3D model atmosphere. *Sol. Phys.* **268**, 255 (2011).
43. Asplund, M., Grevesse, N. & Sauval, A. J. *The Solar Chemical Composition*. (eds Barnes, T. G. & Bash, F. N.) Astronomical Society of the Pacific Conference Series 336, 25 (ASP, 2005).
44. Grevesse, N. & Sauval, A. J. Standard solar compositon. *Space Sci. Rev.* **85**, 161 (1998).
45. Grevesse, N. & Noels, A. in *Origin and Evolution of the Elements* (eds Prantzos, N., Vangioni-Flam, E. & Casse, M.) 15 (Cambrige Univ. Press, Cambridge, 1993).
46. Franco, D., Consolati, G. & Trezzi, D. Positronium signature in organic liquid scintillators for neutrino experiments. *Phys. Rev. C* **83**, 015504 (2011).
47. Geant4. A simulation toolkit. https://geant4.web.cern.ch/ (2018).
48. Bahcall, J. N. & Pena-Garay, C. Solar models and solar neutrino oscillations. *New J. Phys.* **6**, 63 (2004).
49. Blennow, M. & Coloma, P. Quantifying the sensitivity of oscillation experiments to the neutrino mass ordering. *J. High Energy Phys.* **03**, 028 (2013).

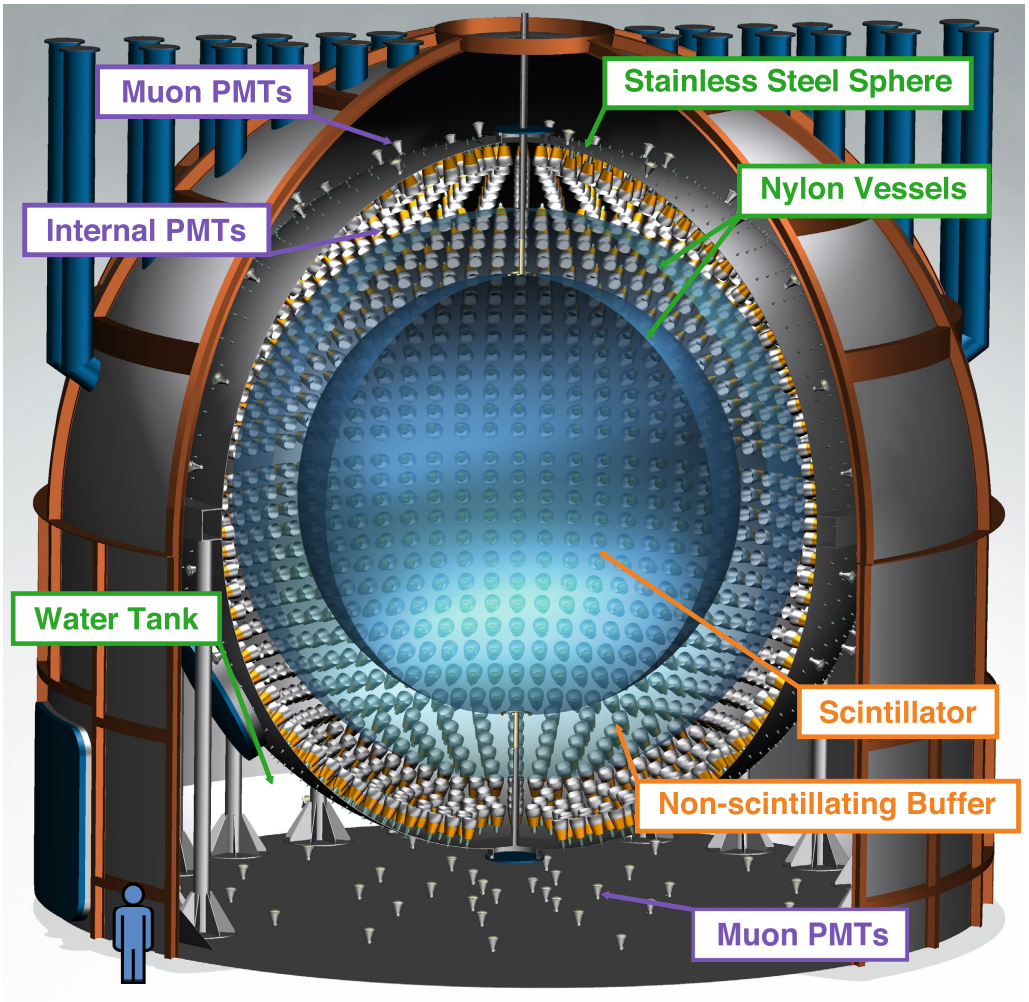

Extended Data Fig. 1 | The Borexino detector. Schematic view of the 'onion-like' structure of the Borexino apparatus. From outside to inside: the external water tank; the Stainless Steel Sphere, where about 2,200 photomultiplier tubes (PMTs) are mounted; the outermost nylon vessel, which serves as a barrier against radon; the innermost nylon vessel, which contains 300 t of liquid scintillator, the active detection medium.

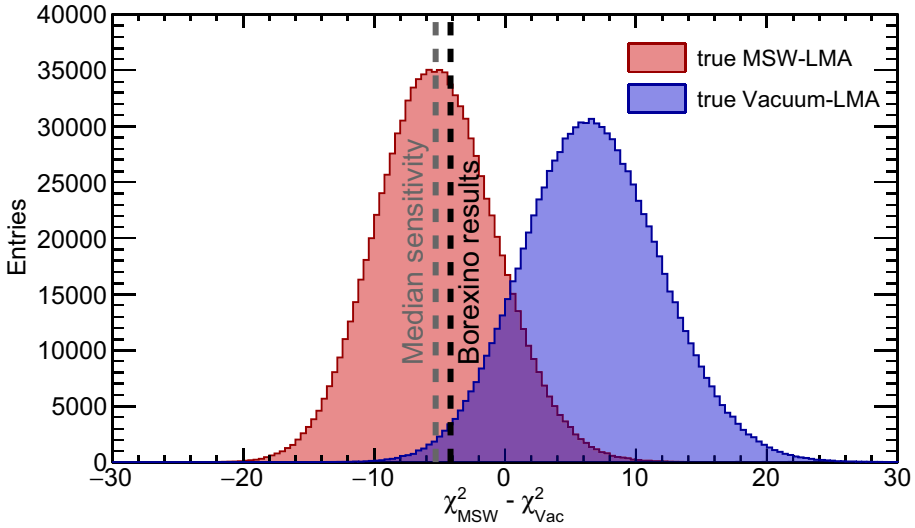

Extended Data Fig. 2 | Frequentist hypothesis test of MSW-LMA versus vacuum-LMA. The probability distribution of the test statistics t is obtained by simulating thousands of sets of P_{ee} values (at the *pp*, ^{7}Be, *pep* and ^{8}B energies) in the MSW-LMA hypothesis (red curve on the left) and in the vacuum-LMA hypothesis (blue curve on the right). The dotted black line corresponds to the results of Borexino discussed in the main text.

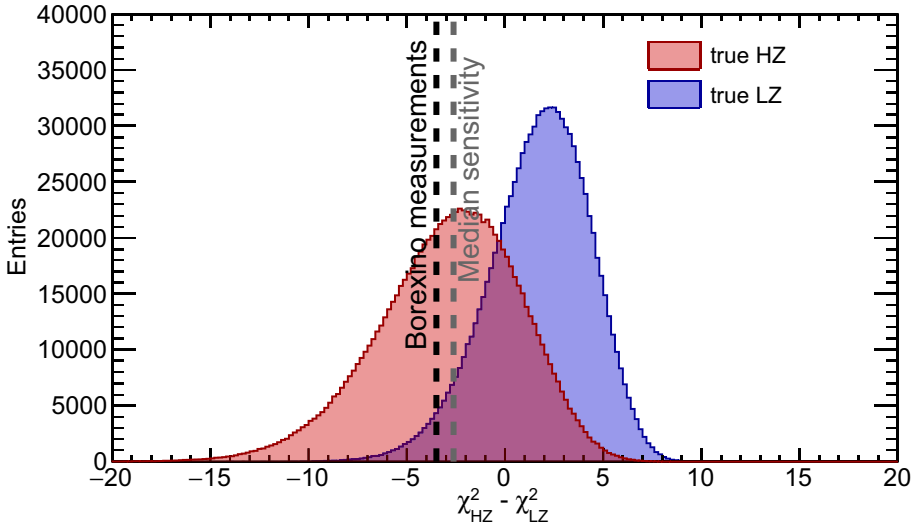

Extended Data Fig. 3 | Frequentist hypothesis test for LZ and HZ. The probability distribution of the test statistics *t* is obtained by simulating thousands of fake sets of ^{8}B–^{7}Be values in the HZ hypothesis (red curve on the left) and in the LZ hypothesis (blue curve on the right). The dotted black line corresponds to the results of Borexino discussed in the main text.

Extended Data Table 1 | LER analysis systematics

	pp neutrinos		^{7}Be neutrinos		*pep* neutrinos	
Source of uncertainty	**-%**	**+%**	**-%**	**+%**	**-%**	**+%**
Fit models (see text)	-4.5	+0.5	-1.0	+0.2	-6.8	+2.8
Fit method (analytical/Monte Carlo)	-1.2	+1.2	-0.2	+0.2	-4.0	+4.0
Choice of the energy estimator	-2.5	+2.5	-0.1	+0.1	-2.4	+2.4
Pile-up modeling	-2.5	+0.5	0	0	0	0
Fit range and binning	-3.0	+3.0	-0.1	+0.1	-1.0	+1.0
Inclusion of the ^{85}Kr constraint	-2.2	+2.2	0	+0.4	-3.2	0
Live time	-0.05	+0.05	-0.05	+0.05	-0.05	+0.05
Scintillator density	-0.05	+0.05	-0.05	+0.05	-0.05	+0.05
Fiducial volume	-1.1	+0.6	-1.1	+0.6	-1.1	+0.6
Total systematics (%)	**-7.1**	**+4.7**	**-1.5**	**+0.8**	**-9.0**	**+5.6**

Relevant sources of systematic uncertainties and their contributions to the measured neutrino interaction rates for the LER analysis.

Extended Data Table 2 | HER analysis systematics

	HER-I		*HER-II*		*HER* (tot)	
Source of uncertainty	**-%**	**+%**	**-%**	**+%**	**-%**	**+%**
Target mass	-2.0	+2.0	-2.0	+2.0	-2.0	+2.0
Energy scale	-0.5	+0.5	-4.9	+4.9	-1.7	+1.7
z-cut	-0.7	+0.7	0	0	-0.4	+0.4
Live time	-0.05	+0.05	-0.05	+0.05	-0.05	+0.05
Scintillator density	-0.05	+0.05	-0.05	+0.05	-0.05	+0.05
Total systematics (%)	**-2.2**	**+2.2**	**-5.3**	**+5.3**	**-2.7**	**+2.7**

Relevant sources of systematic uncertainties and their contributions to the measured neutrino interaction rates for the HER analyses.